Volume 4
Number 10
October 2025
Pages 1203–1314

# Energy Advances

rsc.li/energy-advances

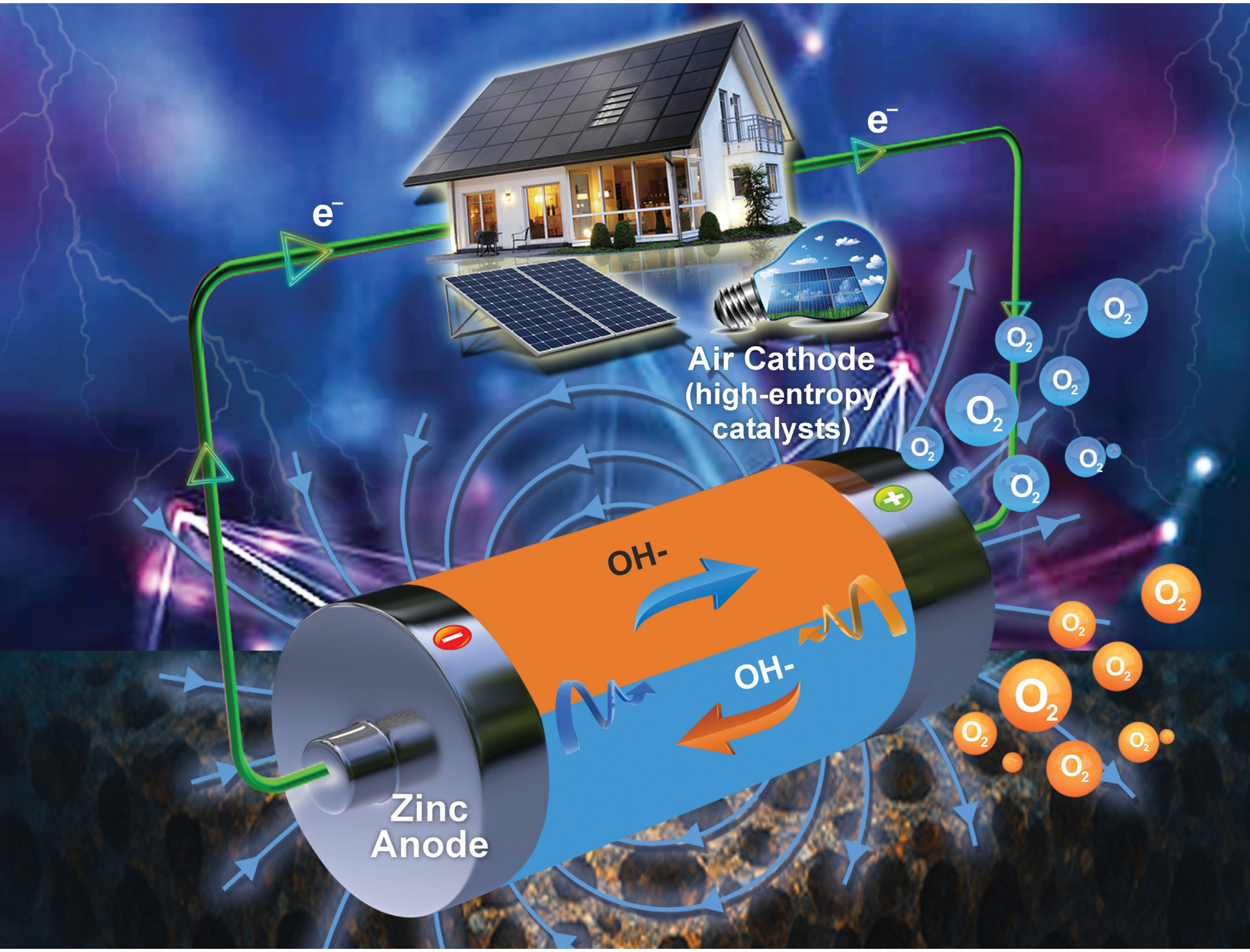

ISSN 2753-1457

ROYAL SOCIETY
OF CHEMISTRY

**PAPER**

Héctor D. Abruña, Dean H. Barrett, Kenneth I. Ozoemena *et al.*
Magnetic enhancement of high-entropy oxide electrocatalysts for high areal-energy rechargeable zinc air batteries

Energy Advances

ROYAL SOCIETY OF CHEMISTRY

PAPER

View Article Online
View Journal | View Issue

Check for updates

Cite this: *Energy Adv.*, 2025, 4, 1229

# Magnetic enhancement of high-entropy oxide electrocatalysts for high areal-energy rechargeable zinc air batteries†

Ernst H. Hechter, [a] Aderemi B. Haruna, [a] Xiao-Yu Yang, [ab] Maxwell W. Terban, [c] Héctor D. Abruña, *[d] Dean H. Barrett *[a] and Kenneth I. Ozoemena *[a]

Received 4th April 2025,
Accepted 23rd July 2025

DOI: 10.1039/d5ya00091b

rsc.li/energy-advances

High-entropy spinel oxide $(Cu_{0.2}Co_{0.2}Fe_{0.2}Mn_{0.2}Ni_{0.2})_3O_4$ nanoparticles were synthesized and confined in Vulcan carbon for use as a bifunctional OER/ORR catalyst in a rechargeable zinc–air battery (RZAB). A partially inverted spinel phase with a distorted $O^{2-}$ lattice was found, with metals randomly distributed in $M^{2+}$ and $M^{3+}$ states. Copper was the exception, being found only as $Cu^{2+}$. Strong metal oxide–support interactions were noted, as well as ferromagnetism. The composite exhibited moderate intrinsic catalytic activity, with overpotentials and current densities comparable to those of commercial platinum on carbon catalysts even at low loadings: an example being $E_{j=10}$ of 1.53 V. Magnetic enhancement was noted and associated with the final OER and initial ORR electron transfers. The performance of the test RZAB was greatly improved when an external magnetic field was applied, with peak power increasing from 101 to 169 mW $cm^{-2}$. We report the most significant magnetic enhancement in the RZAB power profile in the literature to date, as well as improved RZAB stability and areal energy, achieving 43.2 mWh $cm^{-2}$ for over 140 h during 36 h charge–discharge cycles. This work offers insights into the mechanism of magnetic enhancement in the case of high-entropy materials, and illustrates the use of combined strategies to achieve stable, cost-efficient, and effective bifunctional OER/ORR electrocatalysis.

## Introduction

Faced with supply restrictions, the loss of ecosystem services, public health crises and the looming threat of climate change, society has been forced to begin the transition from fossil fuels towards sustainable energy sources.[1] However, storage for intermittent power sources and for vehicles, and the conversion of industries like steel manufacture, remain challenging.[2] The main commercial storage technology, Li-ion batteries, is hindered by the high cost and accessibility of lithium, the requirement for toxic and expensive non-aqueous electrolytes, supply chain vulnerabilities, and a rapidly approaching energy density ceiling. An alternative may be found in metal–air batteries.[3–6] These devices store energy in the potential between atmospheric oxygen and an elemental metal. A rechargeable zinc–air battery (RZAB) uses low cost and abundant zinc metal, and employs a safe, aqueous electrolyte. Since the atmosphere supplies oxygen, a bulky cathode compartment is not required, resulting in a more compact battery pack.

The appeal of zinc–air batteries is evident: zinc is plentiful, the aqueous alkaline electrolytes are benign, and the theoretical energy density of zinc–air batteries is up to five times greater than that of lithium ion batteries, with costs per kWh of storage up to 40 times lower.[4,7]

The main barrier facing RZABs is the bifunctional air cathodes, which currently require high overpotentials and noble metal catalyst combinations to yield acceptable currents.[4,6,7] Adsorption of reactants and desorption of products is a well investigated problem, with the ORR and OER having opposite requirements.[8] Additionally, the OER and ORR involve spin state changes: oxygen has a triplet ground state, while hydroxide and water are both singlets, with no unpaired electrons. Changes from triplet to singlet or *vice versa* are quantum mechanically forbidden. A catalyst is vital for facilitating a

---

[a] *Molecular Science Institute, School of Chemistry, University of the Witwatersrand, Johannesburg 2050, South Africa. E-mail: dean.barrett1@wits.ac.za, Kenneth.ozoemena@wits.ac.za*

[b] *State Key Laboratory of Advanced Technology for Materials Synthesis and Processing, School of Materials Science and Engineering, Wuhan University of Technology, Wuhan 430070, China*

[c] *Max Planck Institute for Solid State Research, Heisenbergstr. 1, 70569 Stuttgart, Germany*

[d] *Department of Chemistry and Chemical Biology, Cornell University, Ithaca, New York 14853, USA. E-mail: hda1@cornell.edu*

† Electronic supplementary information (ESI) available. See DOI: **https://doi.org/10.1039/d5ya00091b**

reaction pathway that leads directly to and from triplet oxygen, through a series of allowed transitions.[9] Currently, rare precious metal catalyst combinations such as ruthenium or iridium oxide and platinum-on-carbon are used to improve the rates of OER and ORR, respectively. The facilitation of spin state change through spin–orbit coupling – that is, the magnetic interactions between the electrons and the nuclei – is one of the reasons why these precious metal catalysts are so active for the oxygen reactions: spin–orbit coupling allows nonradiative excitation and relaxation and hence spin state changes while conserving angular momentum. Spin–orbit coupling becomes more significant as $Z^4$, where $Z$ is the atomic number, making it far more significant for precious metals than for 1st row transition elements which are the preferred catalyst candidates. Ensuring that electrons of the appropriate spin interact in both reductive and oxidative processes – called spin selection – requires a way to bias the spin direction, such as a chiral environment[10] or magnetism.[9,11,12] These requirements pose challenges for traditional methods and materials.[4,5,13,14] Breakthroughs may require combinations of novel methods.

A class of materials that have only recently been investigated as electrocatalysts, but that may have the requisite properties for OER/ORR bifunctionality, are high-entropy oxides. The concept of high-entropy materials (HEMs) was first introduced by Cantor *et al.* and Ye *et al.*, as materials with five or more metals in equimolar proportions, giving them a configurational entropy greater than $1.5R$ and giving rise to four unique effects.[15,16] The "high entropy effect" refers to the spontaneous formation of single-phase solid solutions at sufficiently high temperatures, due to the increased entropy in a solid solution. In these solid solutions, the cation positions of the crystal structure, such as in the spinel structure investigated in this study, are randomly occupied by the metals. The "sluggish diffusion" effect is the extremely slow diffusion of species through the structure, as the randomly positioned metal ions create deep potential wells and steep energy barriers, effectively fixing the solid solution in a metastable state even at low temperatures and under a variety of conditions. The "lattice distortion" effect arises from differences in the sizes and metal–oxygen bond lengths between the ions, causing increased strain, distortion and defects in the crystal structure, as well as altering the electronic band structure of the material. Finally, the "cocktail" effect is the synergistic effects of many metals in close proximity to one another, giving rise to unique active sites.[17–21] This cocktail effect can be seen in other classes of materials, such as multiple metal single atom catalysts, where interactions between metals enable enhanced activities.[22] In summary, the underlying chemistry of HEMs stems from a variety of factors, including the configurational entropy, lattice distortion and sluggish diffusion, which combine to mitigate the tendency for the phase to separate or decompose. Also, it should be noted that the mixing of multiple principal elements in the formation of HEMs lowers the Gibbs free energy of the solid solution, thus allowing for increased stability.

Another area of research that has been receiving attention in electrocatalysis in recent years is the application of external magnetic fields to enhance the catalyst activity. Magnetic fields have several interesting effects on electrochemical systems. The simplest are the Lorentz and Kelvin forces, which interact with charged and paramagnetic species and influence mass transport in solution and gas bubble formation, respectively.[11,23,24] More significantly, magnetic fields also interact with the electrons of the catalyst, as shown in Fig. S1 (ESI†). It has been proposed that the alignment of electron spins in the catalyst in the presence of a magnetic field, as well as stabilisation of high spin electron states in comparison to low spin states,[25] facilitates initial electron transfer processes between the catalyst and reactant,[9] and selects spins such that unwanted intermediates or activated complexes of unfavourable spin state are avoided.[26]

In this work, high entropy spinel oxide $(Cu_{0.2}Co_{0.2}Fe_{0.2}Mn_{0.2}Ni_{0.2})_3O_4$ with crystal structure Fig. S2 (ESI†) (abbreviated as HESOx from here on) nanoparticles were synthesized as shown in Fig. S3 (ESI†), characterised and confined in a network of conductive Vulcan carbon to form a composite material (HESOx/C). Spinel materials are generally good candidates for ferromagnetism, as in magnetite. For OER, iron and cobalt oxides show an optimum adsorption energy for reactants and products, while manganese oxides and nickel oxides show slightly stronger or weaker than ideal binding energies, respectively.[27,28] Their combination is therefore promising, as they could form active sites that both strongly adsorb reactants and easily release products. For example, binary oxides of iron, cobalt and nickel have exhibited good OER activity.[8] For ORR, copper binds oxygen most weakly (closest to the optimum binding energy where platinum and palladium are found) with Ni, Co and Fe binding oxygen progressively more strongly.[8] This enables active sites where good reactant adsorption and good product desorption can be combined. As an inverse spinel oxide $(Cu_{0.2}Co_{0.2}Fe_{0.2}Mn_{0.2}Ni_{0.2})_3O_4$, half of the $M^{3+}$ (*i.e.*, $Co^{3+}$, $Fe^{3+}$, $Mn^{3+}$ and $Ni^{3+}$) are expected to occupy the tetrahedral sites, while the other half along with $M^{2+}$ (*i.e.*, $Cu^{2+}$, $Co^{2+}$, $Fe^{2+}$, $Mn^{2+}$ and $Ni^{2+}$) occupy the octahedral sites. These ions have approximately similar size, and are all expected to take a high spin state in the weak ligand field of the oxygen lattice. Ni is expected to have a greater field stabilisation energy in octahedral sites, but has greater magnetic susceptibility in tetrahedral sites, and so should also be found in both sites as both $Ni^{2+}$ and $Ni^{3+}$.[29] Cu should be found only as $Cu^{2+}$, and its distribution between sites will depend on the inversion of the spinel.[30]

The use of carbon confinement further stabilises high surface areas, enhances conductivity, and modulates the surface chemistry of the HESOx. Altogether, HESOx/C should exhibit good reactant and product binding energies, a distorted lattice promoting active electrons for catalysis, richness in reactive oxygen defects, electronic conductivity, and ferromagnetic properties suitable for enhancement by an external magnetic field.

## Results and discussion

### Physicochemical characterization

ICP-AES analysis (Table S1, ESI†) was used to determine the stoichiometry of HESOx as $(Cu_{0.063}Mn_{0.292}Fe_{0.139}Ni_{0.231}Co_{0.275})_3O_4$, showing that copper content is significantly reduced compared to the other four metals. This is likely due to the strain of Jahn–Teller distortion in $Cu^{2+}$ centred octahedra and tetrahedra, which makes the inclusion of copper in the HESOx structure energetically unfavourable as suggested by Wang *et al.*[31]

Synchrotron powder X-ray diffractograms (PXRD) were collected along with X-ray total scattering measurements at the Canadian light source and European synchrotron and radiation facilities, respectively. The instrumental profile for the diffraction measurements was determined by Rietveld refinement to the LaB6 NIST 660b reference standard at a wavelength of 0.819308 Å. In the HESOx structure, five cation substitutions are possible on the two available crystallographic sites, namely the octahedral and tetrahedral sites. These substitutions produce complex distributions resulting in partial or total inversion of the structure.[32,33] Two distinct sets of reflections could be identified indicating two different spinel-type structures present with different lattice parameters, similar to the approach used by Riley *et al.*[33] The Rietveld refinements of the pristine HESOx and 20% HESOx/C are shown in Fig. 1. Table S2 (ESI†) lists the results of the Rietveld refinements for each composition.

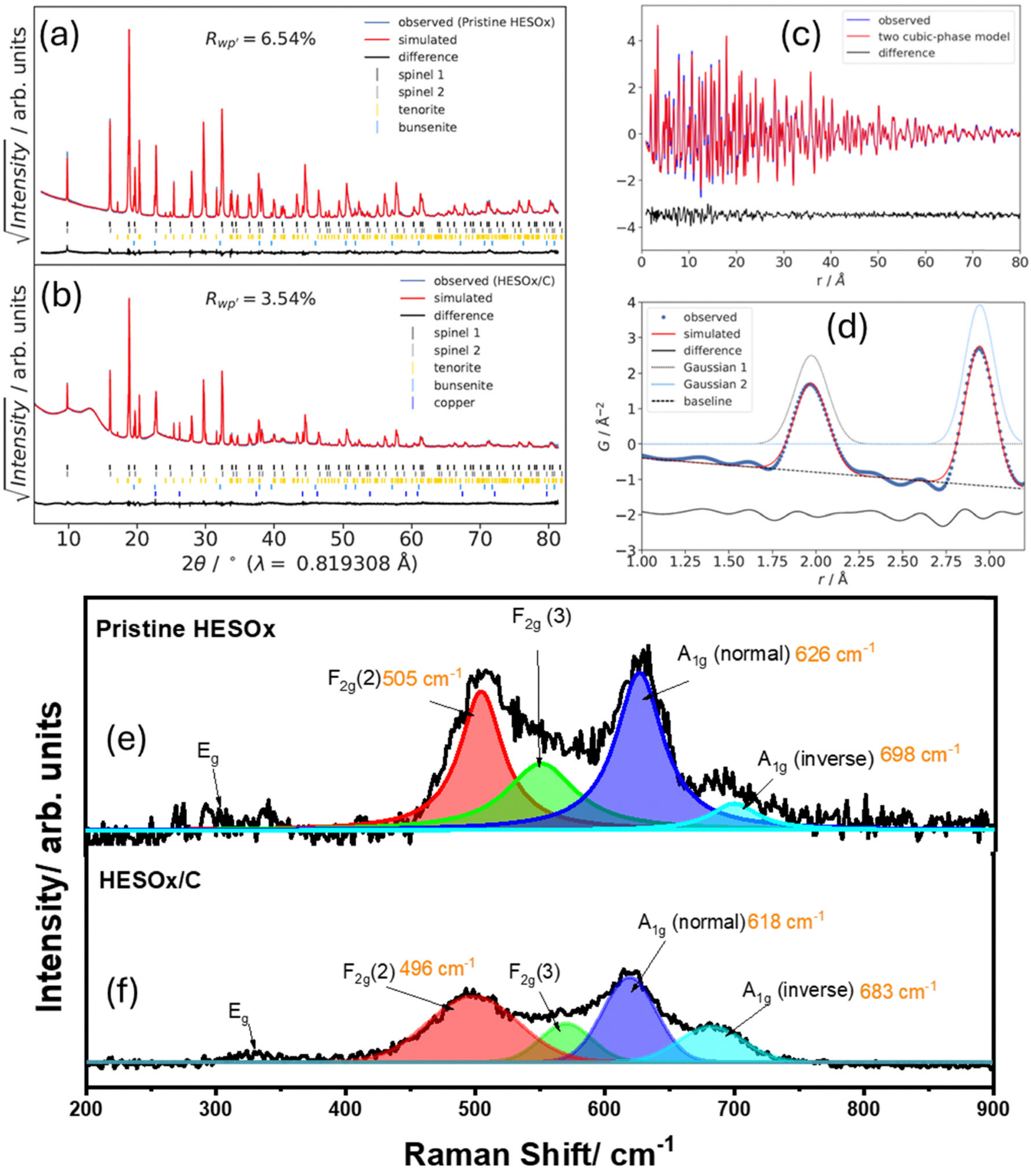

Fig. 1 PXRD of the HESOx and composite with associated Rietveld refinement results for (a) pristine HESOx and (b) 20% HESOx/C. (c) PDF refinements showing the two cubic phase model fitting. (d) Pair distribution function of the metal–oxygen (M–O) and metal–metal (M–M) bond distances (M–O mean 1.9787(14) Å and M–M mean 2.9451(8) Å). Raman spectra showing the lattice vibrations in (e) pristine HESOx and (f) HESOx/C.

The HESOx is structurally similar to a regular metal oxide inverse spinel (COD ID 9006189).[34] Two distinct spinel-type phases provide the best Rietveld fit (Fig. 1(a) and (b)). By comparison of the phase percentages in Table S2 (ESI†), it can be seen that the pristine HESOx is 38% spinel 1, while the composite is 45% spinel 1. Additionally, NiO (bunsenite) and CuO (tenorite) are present due to the expulsion of Ni and Cu from the parent structure.[35] Fcc-type Cu was also observed, providing some metallic Cu. Electronically connected $Cu^{2+}$ and $Cu^0$ atoms may provide increased ORR activity, as is the case in some laccases.[36]

X-ray total scattering data were collected for the HESOx, and the resulting pair distribution function (PDFs) was extracted as shown in Fig. 1(c). The PDF and subsequent fitting support the observation of two distinct spinel-type phases in the pristine HESOx, having $R_w = 11.35$ with 15 parameters, finding the relative phase fractions of the two spinels to be 38% and 49%, supporting the PXRD Rietveld refinement. The first two coordination spheres of the material are shown in Fig. 1(d). These were assigned to the metal–oxygen bond distance as the shortest distance, and metal–metal distances as the next shortest. Interestingly, the metal–oxygen bonds show a broader peak, indicating greater variation in these bond lengths than in the metal–metal distances. This shows that despite the chemical variation causing a larger distribution of M–O bond lengths, the positions of the metal centres do not deviate greatly from the parent spinel structure. These deviations are expected to occur in a multi-cationic material where the sites are randomly occupied by the five metals, each with differing atomic radii. Furthermore, refinements show the most significant deviations from single cubic phase spinel at the higher ends ($r$) of these first two peaks (Fig. S4, ESI†): these are primarily local distortions. Jahn–Teller distortion is perhaps the source, causing antagonistic metal–oxygen bond expansions and contractions which act to broaden the metal–oxygen bond length distribution without affecting the metal–metal distances to the same extent, as found by Rák *et al.*[37] This indicates distortion in the oxygen substructure to accommodate the various metal–oxygen bond lengths, causing increased lattice strain in the oxygen lattice as was found in high-entropy rock salts.[38] Such strain in the oxygen lattice modifies the electronic band structure, which is one of the primary benefits of high entropy material catalysts. Of particular interest, the density of states near the Fermi level may increase, providing more active electrons to participate in the OER/ORR reactions.[39]

Raman spectroscopy (Fig. 1(e) and (f)) reveals three expected peaks: symmetric $A_{1g}$, $3F_{2g}$ and $E_g$ peaks are seen in any spinel.[30] However, an interesting split in the $A_{1g}$ peak is observed. In spinels, the $A_{1g}$ peak is associated with the symmetric vibrations of the tetrahedra. A normal spinel consists of $M^{3+}$ ions in octahedral voids and $M^{2+}$ ions in tetrahedral voids, while inverse spinels have $M^{3+}$ ions in tetrahedral voids and a mix of valencies in the octahedral voids. In normal spinels, where the cation has a 2+ charge, it is found at approximately 610 $cm^{-1}$. In inverse spinels, where the tetrahedral voids in the $O^{2-}$ lattice are occupied by $M^{3+}$ ions, the $A_{1g}$ peak is found around 700 $cm^{-1}$.[40] The difference in the Raman shift can be linked to the strength and bond length of the metal–oxygen interaction in the tetrahedral sites. For HESOx, both peaks are present in Fig. 1(e) and (f), suggesting that the structure has mixed valency in the tetrahedral sites. That high-entropy spinels can have this "partial inversion" has been observed in chromium-containing analogues of the HESOx under investigation here. Comparison between HESOx and its zinc and chromium containing analogues is shown in Table S3 (ESI†). The two $A_{1g}$ peaks are well resolved in this case, since the five metals have similar atomic weights, and so the main factor in the Raman shift is the oxidation state of the metals. This partial inversion provides a natural interpretation of the two spinel phases found in the diffraction and total scattering data. A direct comparison of the Raman peak areas, following the approximation suggested by Modi *et al.*[40] reveals an increase in the degree of inversion from 15% to 34% between the HESOx and HESOx/C. These percentages deviate from those seen in PXRD, since tenorite has an $A_g$ vibration at 630 $cm^{-1}$ which could not be distinguished from the normal spinel $A_{1g}$ vibration and so leads to an underestimate of the degree of inversion. However, the increase in degree of inversion seen upon composite formation allows a tentative assignment of spinel 1 from Table S2 (ESI†) to inverse spinel, and spinel 2 to a normal spinel. Higher ratio of oxidised, low coordination metal sites enhances the adsorption of the electron rich reactants of both the OER and ORR, but limits the desorption of the products. As long as adsorption remains the limiting step, as suggested by the later electrochemistry, a higher degree of inversion is preferred, and inversion tuning may be a promising strategy for the design of future HESOx catalysts. Of further interest is the shift to lower wavenumbers in the $F_{2g}$ and $A_{1g}$ peaks of the composite. This can be attributed to an increase in oxygen defect concentration, which has been linked to better catalytic activity.[41] The increase in oxygen defects may be due to the higher surface area of HESOx particles stabilised in nanopockets in the carbon matrix.

Furthermore, Raman spectroscopy in Fig. S5 (ESI†) reveals an increase in the $I_d/I_g$ ratio of the carbon upon composite formation. The increased $sp^3$ hybridised carbon indicates strong metal oxide–support interactions (SMOSIs) such as covalent bonds between the oxide and support, improving stability and charge transfer between the HESOx and carbon.[42]

SEM images of the two complexes are shown in Fig. S6 (ESI†) with no significant differences in the morphology. Transmission electron microscopy shown in Fig. 2(a) reveals that the HESOx nanoparticles are hexagonal, ranging in size from 50 to 100 nm. The high-resolution TEM in Fig. 2(b) shows the regular crystal HESOx, and Fig. 2(c) shows that it is the (311) face on the hexagonal surfaces. Fig. 2(d) shows the large (dark) HESOx particles embedded in the carbon network. From Fig. 2(e) the interface between HESOx and carbon can be seen: a layer of carbon adheres to the HESOx, due to the SMOSIs indicated by the Raman spectroscopy. The elemental mapping shown in Fig. 2(g)–(l) shows that the concentrations of metals are very

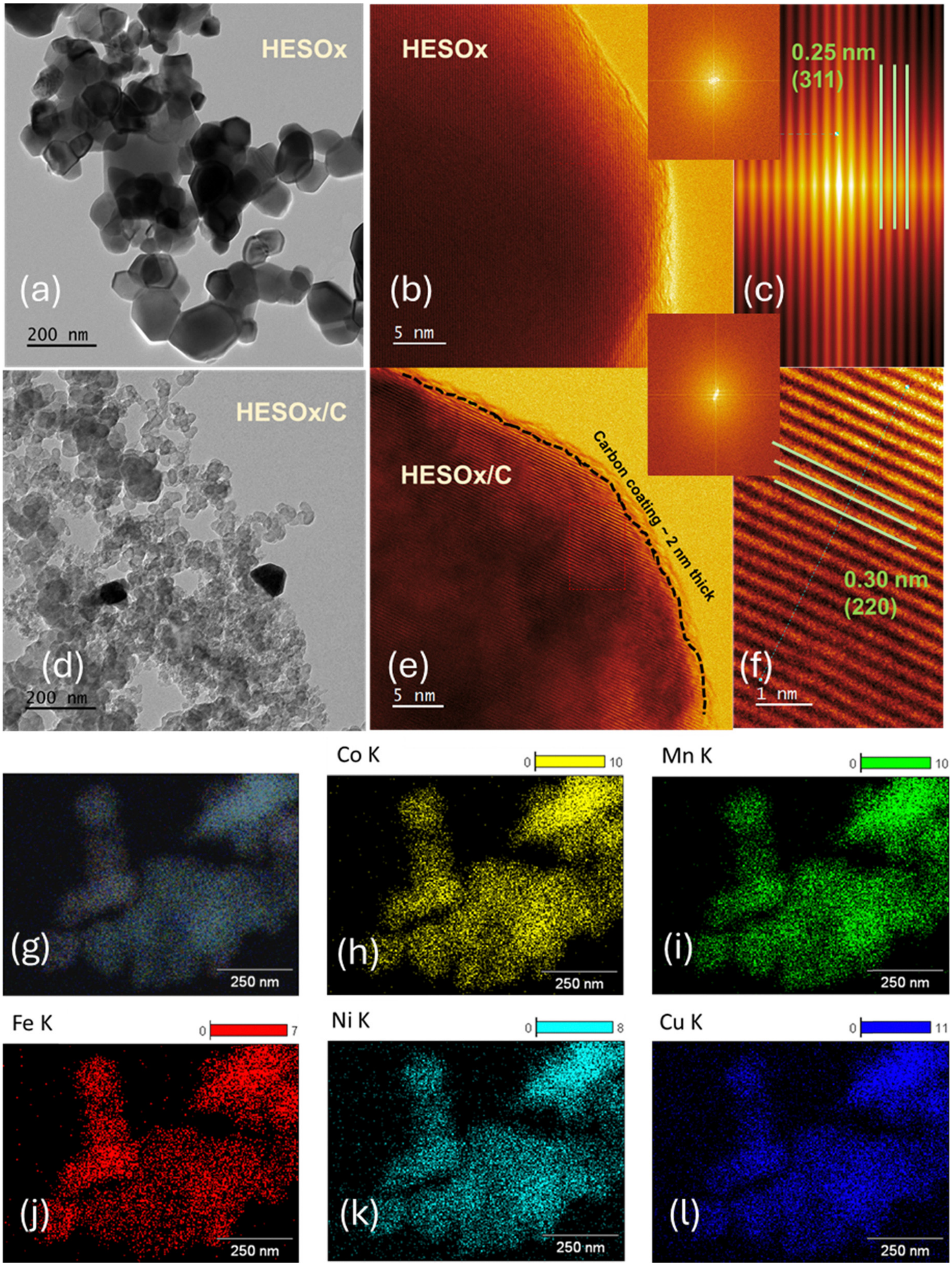

Fig. 2 (a) TEM micrograph of HESOx. (b) HRTEM micrograph of HESOx crystal. (c) Lattice planes extracted from (b) by Fourier transform. (d) TEM micrograph of HESOx/C. (e) HRTEM micrograph of HESOx crystal in carbon network. (f) Lattice planes extracted from (e) by Fourier transform. (g) Combined elemental mapping with cobalt in yellow, manganese in green, iron in red, nickel in cyan and copper in blue. The individual elements are mapped in (h)–(l), respectively.

well correlated with one another, while a mixture of phases would more likely give regions dominated by a single element.

The XPS survey scan (Fig. S7, ESI†) shows all the expected component elements. The deconvoluted XPS spectra are shown in Fig. 3(a)–(f). The metal cations appear to be distributed mainly between the $M^{2+}$ and $M^{3+}$ oxidation states. The prominent satellite peaks around 787 eV in the cobalt spectrum indicate $Co^{2+}$ in octahedral sites.[43] This peak becomes more prominent in the composite, without changes to the $Co^{2+}$ and $Co^{3+}$ signals. This indicates a change in the environment of surface cobalt ions due to the SMOSI, as additional carbon species coordinate to cobalt. Furthermore, the $Co^{2+}$ peak shows a slight shift to lower binding energy due to greater electron density donation from carbon. The Fe $2P_{3/2}$ XPS spectra also show that both $Fe^{2+}$ and $Fe^{3+}$ are present,[44] and a clear shift to lower binding energies in the composite indicates a greater contribution from octahedral coordination and electron density donation from carbon. The two Cu $2p_{3/2}$ signals may be assigned to tetrahedral and octahedral $Cu^{2+}$ sites at the higher and lower binding energies, respectively.[45] $Mn^{2+}$ becomes more prominent in the composite, indicating reduction during composite synthesis. The shake-up peak also becomes more prominent, once again indicating a greater contribution from octahedral coordination around the $Mn^{2+}$. Ni is the only metal showing signs of oxidation on composite formation. The $Ni^{3+}$ signal shifts from 855.9 eV in the HESOx to 857.6 eV in the composite, consistent with a greater contribution from less coordinated, less electron-rich $Ni^{3+}$. According to the d-band center theory, the shift to higher binding energy indicates a weak d-band center (*i.e.*, weak adsorption of oxygen intermediates) that permits enhanced ORR/OER activities. Also, NiOOH is a species often associated with OER catalysis[46,47] is indicated by a small peak at 864 eV. This oxyhydroxide likely contributes to the strengthened oxygen defect signal in the O 1s spectrum of the composite. The oxyhydroxide formation may explain why Ni deviated from the trend towards octahedral coordination seen in the other metals. $Cu^{2+}$ should undergo Jahn–Teller distortion.[34,37] It has been proposed that this could contribute to the formation of a separate copper oxide phase, as seen from the PXRD.[34] Similar reasoning could explain the formation of the minority Bunsenite phase, as tetrahedral $Ni^{2+}$ also experiences Jahn–Teller distortion. However, high-entropy materials are already characterised by a distorted lattice. Rák, Maria & Brenner found that in high-entropy systems, $Cu^{2+}$ octahedra undergo both Jahn–Teller elongation and the less common Jahn–Teller compression, thereby accommodating the preferred bond lengths of the other metal octahedra.[37] Additionally, high spin $Mn^{3+}$ in an octahedral arrangement also undergoes significant Jahn–Teller distortion,[48] due to degeneracy in the bonding orbitals, but shows no evidence of forming separate phases. Jahn–Teller distortion alone is therefore not an acceptable explanation for the partial copper and nickel oxide segregation. Nickel and copper ions are the smallest of the metals used, and so they may continue to migrate during annealing despite the slow diffusion effect. The thermodynamic preference for separate phases at the temperature used here may be too significant to overcome for truly equimolar HESOx. Reducing the percentage of copper, or excluding it entirely in favour of other metals, may be needed to avoid the formation of additional phases.[34] Owing to the disorder intrinsic to the HESOx, oxygen defects are expected. XPS was further used to examine the oxygen O 1s peak, shown in Fig. 3(f). The peak around 531 eV corresponds to surface oxygen species ($O_2^{2-}/O^-$) from low-coordinated oxygen atoms, where $O^{2-}$ has oxidised to maintain charge neutrality. These are sites of lattice distortion and ion vacancies that may provide interesting active sites.[41,49] It is known that the surface oxygen species are strongly electrophilic and serve as active sites for oxidation processes, including OER.[50–52] The HESOx inherently contains oxygen defects due to lattice distortion and the high temperature synthesis protocol, but the composite shows a stronger $O_2^{2-}/O^-$ peak due to oxidation on the surface, especially at the Ni sites according to the metal XPS analysis. The covalent oxygen C–O peak is also increased, as expected due to the inclusion of Vulcan carbon.[53] The increased M–OH peak may also be due to the exposure of additional surface area. While the $O_2^{2-}/O^-$ peak is often used as an indicator of oxygen defect concentration, the confounding factor of the C–O moieties in the Vulcan carbon means that it would be impossible to conclude on oxygen defects using XPS alone. Electron paramagnetic resonance (EPR) was used to confirm that the composites have a higher oxygen defect concentration.

EPR intensity provides a direct measure of the concentration of paramagnetic species in the sample. $O_2^{2-}/O^-$ is of particular interest as an indicator of the surface defect concentration, generally called oxygen defects or vacancies in the literature.[54,55] Fig. 3(g) shows a dramatic increase in signal intensity upon composite formation, supporting the findings from Raman and photoelectron spectroscopy.[41,56] This is evidence that the composite synthesis stabilises smaller particles and oxidises their surfaces, exposing greater surface area and more surface defects. Of further interest in the EPR spectra is the downfield shift with increasing carbon content, indicating that the HESOx has a magnetic shielding on paramagnetic species. This effect, together with the broadness of the peaks, is evidence for ferromagnetic behaviour in the HESOx,[57] in line with the properties of the spinel oxides. This ferromagnetism is what enables the significant magnetic enhancement seen in the later electrocatalysis tests. In the absence of an external field, different crystallites in the catalyst have their unpaired electrons aligned along random axes, while the external field causes alignment of magnetic domains of different crystallites and so strengthens local magnetic fields. It is also possible that the magnetic field will stabilise high spin species in octahedral environments, further strengthening local fields. The total lack of structure in the spectra may be due to the many chemical environments causing broad, overlapping lines,[58] combined with an exchange narrowing effect as spin relaxation in the disordered HESOx is fast relative to hyperfine coupling effects.[59,60] It is also likely that unpaired spins are delocalised throughout the structure, resulting in an EPR signal that is the average of the environments in the structure. This is seen in

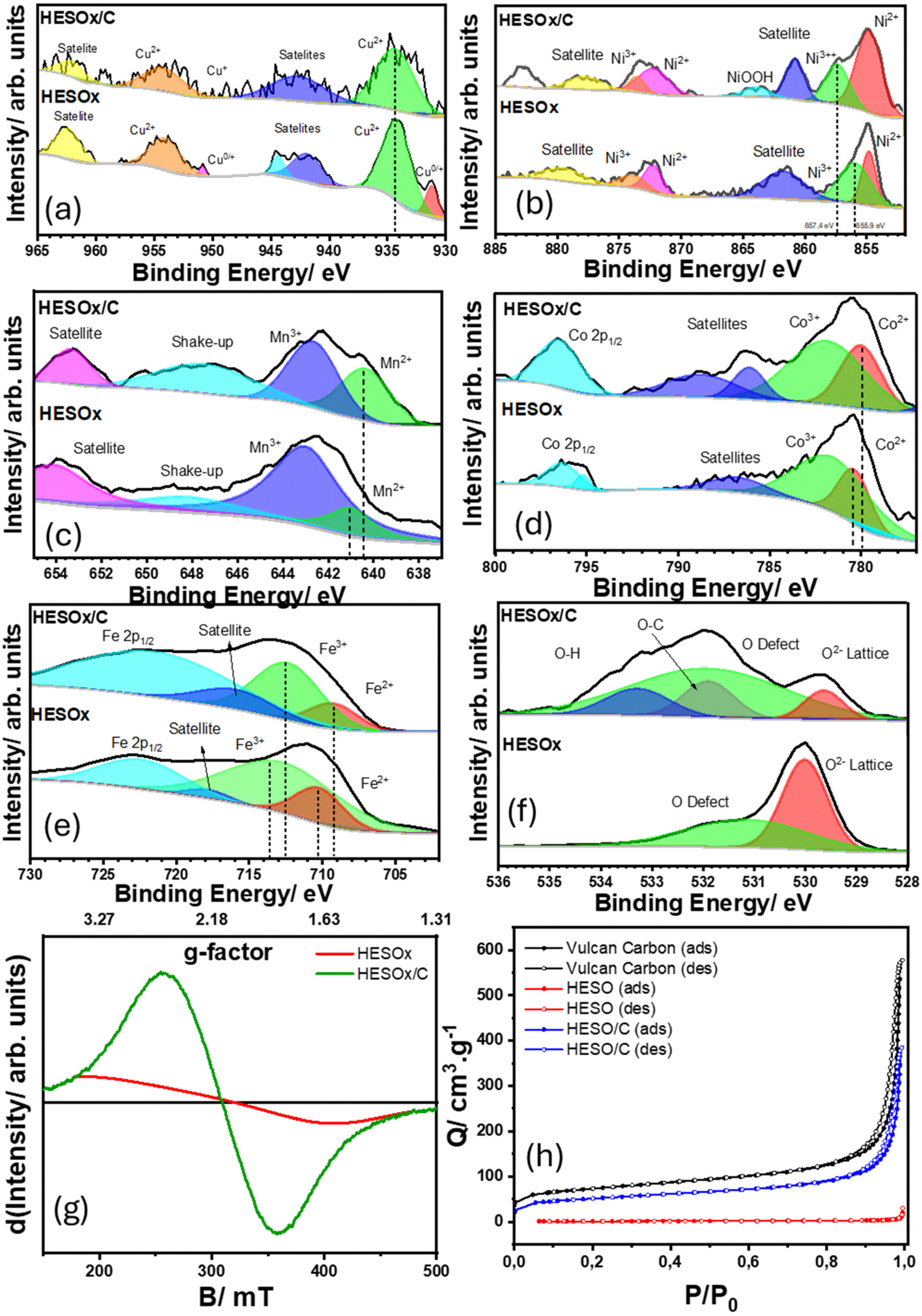

Fig. 3 (a)–(e) shows the deconvoluted 2P XPS spectra of the five metals in both HESOx and HESOx/C. (f) shows the oxygen 1S XPS spectra (g) EPR spectra of HESOx and HESOx/C. (h) $N_2$ absorption–desorption curves.

materials where polaron hopping is the dominant conduction model, as will be elaborated on in the UV-VIS analysis.[60,61]

Surface area analysis using nitrogen adsorption and BET theory can be seen in Fig. 3(h) and Table S4 (ESI†). The poor surface area of the pristine HESOx is obvious, while the composite achieves 182 $m^2$ $g^{-1}$. Thermogravimetric analysis (TGA) (Fig. S8, ESI†) confirms the percentage compositions of the HESOx to the Vulcan carbon.

The Tauc plot in Fig. S9 (ESI†) shows that the pristine HESOx acts as a semiconductor with a moderate band gap of 4.1 eV. The band gap of the pristine material is higher than that of mono and bimetallic spinels, which have optical band gaps between 1 and 3 eV (although optical band gap determination of spinel oxides is somewhat controversial).[62] The diversity in the electronic environments of a high-entropy material can provide a wider range of energy levels, both lower conduction band energies and higher energy valence band energies, but this is not seen in this material.[62,63] It is therefore further evidence that conduction proceeds *via* a polaron-hopping mechanism, where electrons must "hop" from cation to cation, creating a propagating polaron- an electron with an associated phonon as the lattice is distorted by the slow-moving charge. This process is impeded when the donating and receiving cations are of different elements,[64–66] and the high disorder in the HESOx makes it unlikely that electrons can find uninterrupted chains of like-cations. This situation is currently imperfectly modelled, and thus it is difficult to propose strategies to enhance the electron conductivity of the HESOx.[64] The use of conductive supports is therefore essential.

## Electrocatalysis

Results of electrochemical surface area (ECSA) indicate that the composite shows a specific capacitance of 8.1 F $g^{-1}$ (Fig. S10(a), ESI†). The broad redox peak in the cyclic voltammogram ($E_{1/2}$ = 0.71 V *vs.* RHE) (Fig. S10(b), ESI†) indicates that various metals participate in the redox reactions (*i.e.*, $M^{2+}/M^{3+}$, where M = Mn, Co and Fe since Cu is redox-inactive, and Ni redox signature is absent). Fig. S11(a) (ESI†) shows the polarisation curves for the ORR process. $E_{1/2}$ is improved for the chemically mixed composite (*i.e.*, HESOx/C) as compared to the physically mixed composite (*i.e.*, HESOx + C), achieving $E_{1/2}$ of −1.5 mA $cm^{-2}$ or −5.1 A $g^{-1}$ at 0.81 ± 0.02 V *vs.* RHE. Both composites show a bump-like feature before the current decreases to the mass transport-limited current. This may be due to the reduction of Co and/or Mn oxides.

In Fig. S11(b) (ESI†) it can be seen that the onset potential for the OER decreases when the HESOx is mixed with carbon, and improves further when the composite is formed, achieving 10 mA $cm^{-2}$ or 34 A $g^{-1}$ at 1.58 ± 0.02 V, 50 mV earlier than the 1.630 V of commercial $IrO_2$ under the same experimental conditions. This HESOx/C outperforms analogous spinel iron and cobalt oxides,[9] probably due to the multi-active sites offered by the HESOx/C catalyst. The active sites for the OER are generally found on the edge or surface sites on high-index facets of an electrocatalyst. For the HESOx studied in this work, multiple metallic sites should be expected as the active sites. XPS indicates that $O_2^{2-}/O^-$ Ni sites are likely the main OER active sites[51] while Fe and other transition metals play the critical role of activating and stabilising the active sites. Additionally, it should be noted that the surface of the HESOx electrocatalyst can undergo restructuring under applied potential or magnetic field, which can lead to the formation of new active sites. Thus, in the future, the use of advanced level characterisation, such as *in situ* and/or *operando* synchrotron techniques, would be necessary to identify the active sites and allow for a thorough understanding of the interplay between the different types of active sites for OER and ORR.

Electrochemical parameters were investigated with and without a magnetic field using the in-house 3D ReZAB microelectrochemical cell (Fig. S12, ESI†), and setup as shown in Fig. S13 (ESI†). The setup could supply a small effective magnetic field of 20 mT. A correspondingly small magnetic enhancement can be seen in Fig. S11(d) (ESI†), showing the calculated number of electrons transferred in the ORR performed with and without a field. The HESOx/C intrinsically shows $n$ = 3.1, indicating that both the 2 and 4 electron ORR pathways are present. After the field is applied, the calculated electron number increases to 3.9, indicating that the 4-electron pathway is more favoured under the magnetic field. The 4-electron pathway is preferred as it is more energy efficient and does not produce $H_2O_2$ as an intermediate, which can degrade cell components, especially the membrane and ionomer. The ORR Tafel plot in Fig. S11(c) (ESI†) also shows that the applied field decreased the Tafel slope by 10 mV $dec^{-1}$, a modest but definite improvement in energy efficiency. In terms of kinetics, this suggests an increase in the rate of the first electron transfer step (Scheme 1).

This first step, shown in Scheme 1, involves a spin state change, and so the spin alignment effect is expected to be significant. Fig. S11(g) (ESI†) shows an 82 mV $dec^{-1}$ drop in Tafel slope for the OER after application of the field. This is most likely due to a shift in the rate limiting step from a chemical step, which would give a slope above 200 mV $dec^{-1}$ since it is insensitive to applied potential, to an electrochemical one.[67] This could be explained by reaction (4), of Scheme 1 which has both a chemical and an electrochemical component: the reaction between a metal oxyhydroxide and hydroxide is a chemical step: $M\text{–}OOH + OH^- \rightleftarrows M\text{–}OO^- + H_2O$, and is followed by the final oxidation step and then desorption of oxygen. The magnetic field could stabilise the intermediate species, and so slow the reverse reaction (oxyhydroxide formation).

Electrochemical impedance spectroscopy in Fig. S11(e) and (f) (ESI†) only showed the influence of the magnetic field in

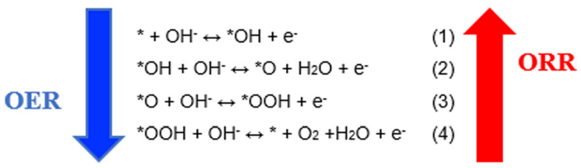

Scheme 1 The four electron transfer reactions of the ORR/OER.

0.1 M KOH. The magnetic field decreased the mass transport resistance slightly from 43.5 ± 0.2 Ω to 42.6 ± 0.2 Ω, while the sum of charge transfer resistances decreased from 33 ± 2 Ω to 29 ± 2 Ω. The equivalent circuit indicates that two distinct surfaces are active for ORR: $R_{CT}$ 1 decreased from 19 ± 1 to 18 ± 1 Ω, while $R_{CT}$ 2 showed a decrease from 14 ± 1 to 12 ± 1 Ω. These two surfaces may be different sublattices or different crystal faces. A similar situation is seen for the OER, with small decreases in both mass transport charge transfer resistances. These improvements are small, and the differences are of the same order as the uncertainties (Table S5, ESI†). However, the fact that all four charge transfer resistances show a small decrease upon application of the field lends evidence that this is not merely experimental error. Overall, the applied magnetic field yields a slight improvement to electron number and charge transfer resistance in the 3-electrode tests, serving as a proof of concept leading into the following 2-electrode tests under a more powerful 160 mT effective magnetic field, using the setup shown in Fig. S13 (ESI†).

Fig. 4(b) shows the power profiles with and without a magnetic field. Without the field, the peak power reached 101 ± 7 mW cm$^{-2}$ at 199 mA cm$^{-2}$. However, with the magnetic field on, the power increased significantly, reaching a peak value of 169 ± 7 mW cm$^{-2}$ at 311 mA cm$^{-2}$. With the magnetic field, the peak power exceeds that of mixed Pt/C and $RuO_2$ or $IrO_2$ RZAB cathodes.[68,69] For completeness, a RZAB with a standard 20% Pt/C + $IrO_2$ cathode was tested with and without an applied magnetic field under the same conditions. Previous studies have excluded their standard cathode from the magnetic field studies,[25,70] perhaps because these materials do not exhibit ferromagnetism or because of findings such as those of Garcés-Pineda *et al.* (2019),[71] where the magnetic field did not affect the OER performance of $IrO_2$ in a three-electrode system. In contrast, we found that 20% Pt/C + $IrO_2$ exhibited a small but noteworthy enhancement in power under a magnetic field, from 103.5 to 113.7 mW cm$^{-2}$. This is due to the paramagnetic $IrO_2$ allowing for a small degree of spin alignment.

As can be seen in the EIS data (Fig. S14 and Table S6, ESI†), magnetism shows enhanced electrochemistry. The electrical equivalent circuit in Fig. S14 (ESI†) represents the electrolyte or mass transport resistance ($R_S$) and electron transfer resistance ($R_{CT}$). After the field is applied, the $R_{CT}$ decreased by 10 Ω, from 20 to 10 Ω. Charge transfer resistance, significantly dependent on spintronic effects at the active sites, is

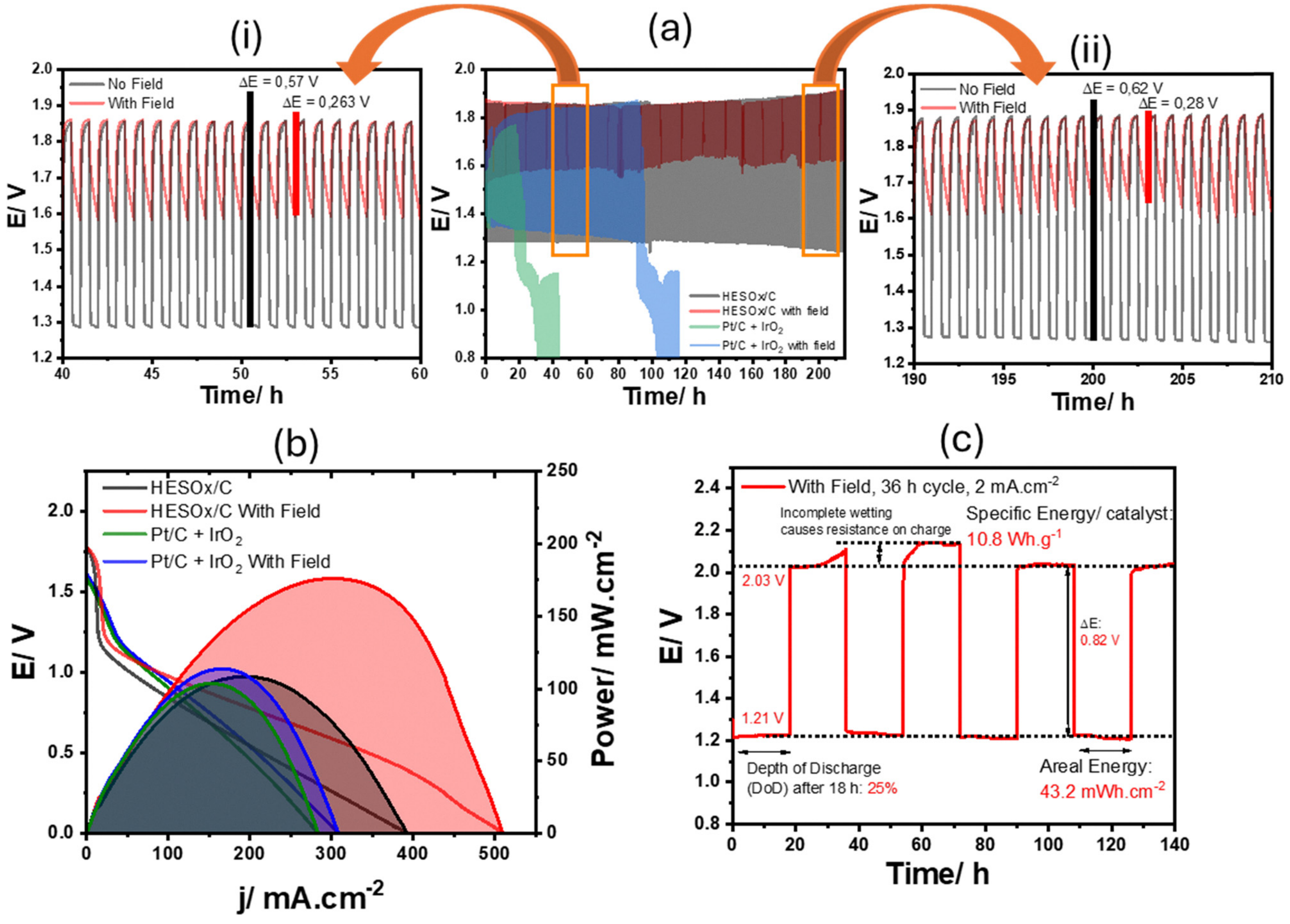

Fig. 4 (a) Discharge profiles of the standards and HESOx/C (1 h cycle, 0.5 mA cm$^{-2}$). Zoomed-in portions of (a) at (i) 50 h and (ii) 200 h. (b) Power profiles of the standard 20% Pt/C + $IrO_2$ cathode and the 20% HESOx/C cathode, with and without an applied field. (c) Deep discharge profile (36 h cycle, 2 mA cm$^{-2}$) of HESOx/C. All data acquired under air.

diminished to a far greater extent in the 2-electrode system due to the more powerful magnetic field. Peculiarly, the mass transport resistance $R_S$ was unchanged in the two-electrode system, as opposed to the small decrease seen in the three-electrode system. The electrolyte is 60 times more concentrated in the RZAB than in the three-electrode test and contains zinc cations in addition to hydroxide anions (anions and cations experience Lorentz forces in opposite directions). It is possible that interfering Lorentz force currents create turbulence, retarding the current through the electrolyte instead of aiding mass transport. It should also be noted that the angle between the magnetic field and the ion current is greater (closer to parallel) in the 2-electrode system than in the 3-electrode system. According the White's group[72] the magnetohydrodynamic enhancement of mass transport is at a maximum when the angle is close to 90, and at a minimum when the field and current are parallel. This effect would also serve to minimise mass transport effects in the 2-electrode system used here, but a cell with a design allowing a perpendicular field could be used to examine which effect dominates the mass transport: interfering Lorentz forces or the angle between field and current.

The results of stability testing are shown in Fig. 4(a) and (c). The magnetic field suppresses the voltage drop compared to the unenhanced RZAB. Without the field, the voltage gap increased from 0.57 V at 50 h to 0.62 V at 200 h, a change of 50 mV. Theoretically, the HESOx particles themselves should resist metal dissolution due to the slow diffusion effect, but some dissolution or surface reconstruction is possible. The main culprits are likely zinc plate passivation and dendrite formation, zincate and potassium carbonate deposition, and oxidation of the carbon matrix, especially by peroxide side products. With the field, the gap increased from 0.26 to 0.28 V over the same length of time, an increase of only 20 mV. The difference is most apparent in the discharge voltage in Fig. 4(a) (i) and (ii), which depends on the ORR. This may be due to what White *et al.* called magnetic focusing due to the Kelvin force. The external magnetic field magnetises the ferromagnetic catalyst, causing a stronger magnetic field near the catalyst. The greater magnetic flux causes an attractive force on paramagnetic species, in this case triplet oxygen, near the surface, and so increases their concentration in the depletion zone.[73] Insufficient oxygen flux was hence prevented by the applied field. The Kelvin force does not affect the EIS measurement, as the alternating electric field does not cause the development of a depletion layer. EIS from before the stability test and from after $\Delta V$ exceeded 1.5 V is shown in Fig. S14 (ESI†). $R_S$ decreased by 1 Ω due to incomplete wetting before the cycling stability test. Charge transfer resistance increased by 14 to 24 Ω. The improved stability under the magnetic field can further be attributed to the Lorentz force convection currents, abstractly shown in Fig. S17 (ESI†), limiting the deposition of zincates and carbonates on the electrodes, mitigating passivation, dendrite formation and the blocking of pores on the cathode. The greater preference for 4-electron processes under the magnetic field seen during the 3-electrode tests also reduces peroxide formation, limiting the oxidation of the carbon support.

It is noteworthy that the charging potentials in the 2-electrode tests, which are mediated by the OER, are not improved under a magnetic field despite the 3-electrode tests' indications that OER is indeed enhanced. This may also be due to the aforementioned magnetic focusing, trapping the evolved triplet oxygen at the active sites, slowing the OER.

The electrochemical data, including the EIS, presented in this work prove that paramagnetic catalysts may be appropriate candidates for magnetic enhancement. To our knowledge, this work gives the most significant magnetic enhancement of a RZAB power reported thus far (see Table S7, ESI†).

## Conclusion

$(CuCoFeMnNi)_3O_4$ high-entropy spinel oxide and a $(CuCoFeMnNi)_3O_4$/Vulcan carbon composite were successfully synthesized. The structure was found to be a partially inverted spinel, and lattice distortion was observed in the anion lattice. The HESOx alone exhibited poor catalytic activity in the ORR and OER due to its low electronic conductivity and surface area, but the composite showed good activity comparable to state of the art bifunctional catalysts with $\Delta E$ = 0.65 V, and outperformed commercial $IrO_2$ as an oxygen evolution catalyst, with $E_{j=10}$ = 1.534 V. The composite's activity is ascribed to increased conductivity, surface area and greater surface concentration of oxygen defects and the associated reactive electrons. The small change in mass transport resistance seen under the magnetic field in the RDE tests suggests that the mass transport mechanism for magnetic enhancement has a definite effect in a real OER/ORR system, despite hydroxide ions propagating through the Grotthuss mechanism. The effect was not seen in the 2-electrode system, likely due to the angle between the magnetic and electric fields being closer to parallel. Mass transport enhancement may be a viable approach in systems where the magnetic field is perpendicular to the electric field. 3-Electrode tests showed that charge transfer was improved by the magnetic field. In particular, the spin-change in reaction (4) seems to be facilitated. The RZAB tests showed that the composite was a viable air cathode catalyst in a real system, and the magnetic field produced an enhancement in power, rate capability and stability, though it did not lower charging voltage due to magnetic focusing of oxygen at the active sites. This study reinforces the appeal of high-entropy materials in electrochemistry and clearly shows that a static magnetic field is a viable approach to enhancing OER/ORR catalysis in various setups. We have demonstrated that combined approaches may be used for the development of functional electrochemistry, for a sustainable, high technology future.

## Conflicts of interest

There are no conflicts to declare.

## Data availability

The data supporting this article have been included as part of the ESI.†

## Acknowledgements

We are grateful to the National Research Foundation (NRF), the Department of Science and Innovation (DSI) Energy Storage Consortium, and the DSI-NRF-Wits SARChI Chair in Materials Electrochemistry and Energy Technologies (MEET) (UID no. 132739). We thank Prof D. Wamwangi of the Wits School of Physics for his valuable insights into magnetism and for providing the magnets for this work. Synchrotron data were acquired through the NRF grant SRUG2204041774. We acknowledge the European Synchrotron Radiation Facility (ESRF) for the provision of synchrotron radiation facilities under proposal MA5435 and the Canadian Light Source under proposals 36G12674 and 37G12950.

## References

1 N. Healy, J. C. Stephens and S. A. Malin, *Energy Res. Soc. Sci.*, 2019, **48**, 219–234.

2 S. Luidold and H. Antrekowitsch, *JOM*, 2007, **59**, 20–26.

3 D. Chao, W. Zhou, F. Xie, C. Ye, H. Li, M. Jaroniec and S.-Z. Qiao, *Sci. Adv.*, 2020, **6**, eaba4098.

4 Q. Liu, Z. Pan, E. Wang, L. An and G. Sun, *Energy Storage Mater.*, 2020, **27**, 478–505.

5 Y. Li and J. Lu, *ACS Energy Lett.*, 2017, **2**, 1370–1377.

6 Y.-L. Zhang, K. Goh, L. Zhao, X.-L. Sui, X.-F. Gong, J.-J. Cai, Q.-Y. Zhou, H.-D. Zhang, L. Li, F.-R. Kong, D.-M. Gu and Z.-B. Wang, *Nanoscale*, 2020, **12**, 21534–21559.

7 H.-F. Wang and Q. Xu, *Matter*, 2019, **1**, 565–595.

8 J. Liu, R. Wang, Z. Chen, N. Hu, X. Chaohe and Z. Shen, *ChemElectroChem*, 2018, **5**, 1745.

9 X. Ren, T. Wu, Y. Sun, Y. Li, G. Xian, X. Liu, C. Shen, J. Gracia, H.-J. Gao, H. Yang and Z. J. Xu, *Nat. Commun.*, 2021, **12**, 2608.

10 A. Gupta, Y. Sang, C. Fontanesi, L. Turin and R. Naaman, *J. Phys. Chem. Lett.*, 2023, **14**, 1756–1761.

11 V. Gatard, J. Deseure and M. Chatenet, *Curr. Opin. Electrochem.*, 2020, **23**, 96.

12 Y. Jiao, R. Sharpe, T. Lim, J. W. H. Niemantsverdriet and J. Gracia, *J. Am. Chem. Soc.*, 2017, **139**, 16604–16608.

13 A. B. Haruna and K. I. Ozoemena, *Curr. Opin. Electrochem.*, 2020, **21**, 219–224.

14 Y. Gorlin, B. Lassalle-Kaiser, J. D. Benck, S. Gul, S. M. Webb, V. K. Yachandra, J. Yano and T. F. Jaramillo, *J. Am. Chem. Soc.*, 2013, **135**, 8525–8534.

15 Y. F. Ye, Q. Wang, J. Lu, C. T. Liu and Y. Yang, *Mater. Today*, 2016, **19**, 349–362.

16 B. Cantor, I. T. H. Chang, P. Knight and A. J. B. Vincent, *Mater. Sci. Eng., A*, 2004, **375–377**, 213–218.

17 T. X. Nguyen, Y.-C. Liao, C.-C. Lin, Y.-H. Su and J.-M. Ting, *Adv. Funct. Mater.*, 2021, **31**, 2101632.

18 M. Fu, X. Ma, K. Zhao, X. Li and D. Su, *iScience*, 2021, **24**, 102177.

19 A. Amiri and R. Shahbazian-Yassar, *J. Mater. Chem. A*, 2021, **9**, 782–823.

20 Y. Sun and S. Dai, *Sci. Adv.*, 2021, **7**, eabg1600.

21 B. Wang, Y. Yao, X. Yu, C. Wang, C. Wu and Z. Zou, *J. Mater. Chem. A*, 2021, **9**, 19410–19438.

22 J.-E. Tsai, W.-X. Hong, H. Pourzolfaghar, W.-H. Wang and Y.-Y. Li, *Chem. Eng. J.*, 2023, **460**, 141868.

23 L. M. A. Monzon, K. Rode, M. Venkatesan and J. M. D. Coey, *Chem. Mater.*, 2012, **24**, 3878–3885.

24 K. Roy, P. Devi and P. Kumar, *Nano Energy*, 2021, **87**, 106119.

25 Y. Wang, Y. Zhang, S. Xia, J. Yu and B. Ding, *Adv. Mater.*, 2021, **33**, 2007525.

26 J. Li, J. Ma, Z. Ma, E. Zhao, K. Du, J. Guo and T. Ling, *Adv. Energy Sustainability Res.*, 2021, **2**, 2100034.

27 F. Song, M. Busch, B. Lassalle, C.-S. Hsu, E. Petkucheva, M. Bensimon, H. Chen, C. Corminboeuf and X. Hu, *ACS Cent. Sci.*, 2019, **5**, 558–568.

28 Y. Xiong and P. He, *J. Mater. Sci.*, 2023, **58**, 2041–2067.

29 P. Porta, F. S. Stone and R. G. Turner, *J. Solid State Chem.*, 1974, **11**, 135–147.

30 B. D. Hosterman, Raman Spectroscopic Study of Solid Solution Spinel Oxides, Doctoral dissertation, UNLV Theses, Dissertations, Professional Papers, and Capstones, 2011, 1087, DOI: 10.34917/2476131.

31 D. Wang, Z. Liu, S. Du, Y. Zhang, H. Li, Z. Xiao, W. Chen, R. Chen, Y. Wang, Y. Zou and S. Wang, *J. Mater. Chem. A*, 2019, **7**, 24211–24216.

32 M. Fracchia, M. Manzoli, U. Anselmi-Tamburini and P. Ghigna, *Scr. Mater.*, 2020, **188**, 26–31.

33 C. Riley, N. Valdez, C. M. Smyth, R. Grant, B. Burnside, J. E. Park, S. Meserole, A. Benavidez, R. Craig, S. Porter, A. DeLaRiva, A. Datye, M. Rodriguez and S. S. Chou, *J. Phys. Chem. C*, 2023, **127**, 11249–11259.

34 Y. Wang, H. Li, H. Liu, L. Yang and C. Zeng, *Ceram. Int.*, 2023, **49**, 1940–1946.

35 H. S. C. O'Neill and W. A. Dollase, *Phys. Chem. Miner.*, 1994, **20**, 541–555.

36 D. Grumelli, B. Wurster, S. Stepanow and K. Kern, *Nat. Commun.*, 2013, **4**, 2904.

37 Z. Rák, J.-P. Maria and D. W. Brenner, *Mater. Lett.*, 2018, **217**, 300–303.

38 C. M. Rost, Z. Rak, D. W. Brenner and J.-P. Maria, *J. Am. Ceram. Soc.*, 2017, **100**, 2732–2738.

39 K. Chen, S. Kim, R. Rajendiran, K. Prabakar, G. Li, Z. Shi, C. Jeong, J. Kang and O. L. Li, *J. Colloid Interface Sci.*, 2021, **582**, 977–990.

40 K. B. Modi, P. Y. Raval, S. J. Shah, C. R. Kathad, S. V. Dulera, M. V. Popat, K. B. Zankat, K. G. Saija, T. K. Pathak, N. H. Vasoya, V. K. Lakhani, U. Chandra and P. K. Jha, *Inorg. Chem.*, 2015, **54**, 1543–1555.

41 Z. Li, Y. Zhang, Y. Feng, C.-Q. Cheng, K.-W. Qiu, C.-K. Dong, H. Liu and X.-W. Du, *Adv. Funct. Mater.*, 2019, **29**, 1903444.

42 F. Lai, J. Feng, T. Heil, G.-C. Wang, P. Adler, M. Antonietti and M. Oschatz, *Energy Storage Mater.*, 2019, **20**, 188–195.

43 J.-G. Kim, D. L. Pugmire, D. Battaglia and M. A. Langell, *Appl. Surf. Sci.*, 2000, **165**, 70–84.

44 S. Ding, J. A. Barr, Q. Shi, Y. Zeng, P. Tieu, Z. Lyu, L. Fang, T. Li, X. Pan, S. P. Beckman, D. Du, H. Lin, J.-C. Li, G. Wu and Y. Lin, *ACS Nano*, 2022, **16**, 15165–15174.

45 J. Flores Lasluisa, J. Quílez-Bermejo, A. Ramírez-Pérez, F. Huerta, D. Cazorla-Amorós and E. Morallon, *Materials*, 2019, **12**, 1302.

46 R. A. Krivina, Y. Ou, Q. Xu, L. P. Twight, T. N. Stovall and S. W. Boettcher, *Acc. Mater. Res.*, 2021, **2**, 548–558.

47 Z. Wang, Y. Wang, N. Zhang, L. Ma, J. Sun, C. Yu, S. Liu and R. Jiang, *J. Mater. Chem. A*, 2022, **10**, 10342–10349.

48 A. B. Haruna, D. H. Barrett, C. B. Rodella, R. M. Erasmus, A. M. Venter, Z. N. Sentsho and K. I. Ozoemena, *Electrochim. Acta*, 2022, **426**, 140786.

49 L. Fu, H. Chen, K. Wang and X. Wang, *J. Alloys Compd.*, 2022, **891**, 161925.

50 N. A. Merino, B. P. Barbero, P. Eloy and L. E. Cadús, *Appl. Surf. Sci.*, 2006, **253**, 1489–1493.

51 E. Gioria, S. Li, A. Mazheika, R. Naumann d'Alnoncourt, A. Thomas and F. Rosowski, *Angew. Chem., Int. Ed.*, 2023, **62**, e202217888.

52 L. Liu, Y. Ji, W. You, S. Liu, Q. Shao, Q. Kong, Z. Hu, H. Tao, L. Bu and X. Huang, *Small*, 2023, **19**, 2208202.

53 A. Moraes, M. H. M. T. Assumpção, F. C. Simões, V. S. Antonin, M. R. V. Lanza, P. Hammer and M. C. Santos, *Electrocatalysis*, 2016, **7**, 60–69.

54 K. Gu, D. Wang, C. Xie, T. Wang, G. Huang, Y. Liu, Y. Zou, L. Tao and S. Wang, *Angew. Chem.*, 2021, **133**, 20415–20420.

55 J. Zhang, H. Liu, Y. Gu, J. Zhang, X. Zhang and X. Qi, *J. Mater. Sci.: Mater. Electron.*, 2022, **33**, 9918–9929.

56 B. Zhang, D. Deng, J. Chen, Y. Li, M. Yuan, W. Xiao, S. Wang, X. Wang, P. Zhang, Y. Shu, S. Shi and C. Chen, *ACS Appl. Mater. Interfaces*, 2023, **15**, 52705–52715.

57 N. J. Usharani, A. Bhandarkar, S. Subramanian and S. S. Bhattacharya, *Acta Mater.*, 2020, **200**, 526–536.

58 R. K. Malhotra, V. P. Seth and V. K. Jain, *Can. J. Phys.*, 1983, **61**, 1359–1361.

59 P. W. Anderson and P. R. Weiss, *Rev. Mod. Phys.*, 1953, **25**, 269–276.

60 J. N. Spencer, A. Folli, H. Ren and D. M. Murphy, *J. Mater. Chem. A*, 2021, **9**, 16917–16927.

61 L. Murawski, C. Gledel, C. Sanchez, J. Livage and J. P. Audières, *J. Non-Cryst. Solids*, 1987, **89**, 98–106.

62 M. Meinert and G. Reiss, *J. Phys.: Condens. Matter*, 2014, **26**, 115503.

63 D. Stenzel, B. Zhou, C. Okafor, M. V. Kante, L. Lin, G. Melinte, T. Bergfeldt, M. Botros, H. Hahn, B. Breitung and S. Schweidler, *Front. Energy Res.*, 2022, **10**, 942314.

64 A. Bhargava, R. Eppstein, J. Sun, M. A. Smeaton, H. Paik, L. F. Kourkoutis, D. G. Schlom, M. Caspary Toroker and R. D. Robinson, *Adv. Mater.*, 2020, **32**, 2004490.

65 Z. Lu, J. Zhu, E. Andrew Payzant and M. P. Paranthaman, *J. Am. Ceram. Soc.*, 2005, **88**, 1050–1053.

66 K. R. Chemelewski, E.-S. Lee, W. Li and A. Manthiram, *Chem. Mater.*, 2013, **25**, 2890–2897.

67 D. Antipin and M. Risch, *Electrochem. Sci. Adv.*, 2023, **3**, e2100213.

68 L. Xu, S. Wu, X. He, H. Wang, D. Deng, J. Wu and H. Li, *Chem. Eng. J.*, 2022, **437**, 135291.

69 Z. Jin, X. Zhou, Y. Hu, X. Tang, K. Hu, K. M. Reddy, X. Lin and H.-J. Qiu, *Chem. Sci.*, 2022, **13**(41), 12056–12064.

70 Z. Zhang, L. Jia, T. Li, J. Qian, X. Liang, D. Xue and D. Gao, *J. Energy Chem.*, 2023, **78**, 447–453.

71 F. A. Garcés-Pineda, M. Blasco-Ahicart, D. Nieto-Castro, N. López and J. R. Galán-Mascarós, *Nat. Energy*, 2019, **4**, 519–525.

72 Y. Yang, K. M. Grant, H. S. White and S. Chen, *Langmuir*, 2003, **19**, 9446–9449.

73 K. M. Grant, J. W. Hemmert and H. S. White, *Electrochem. Commun.*, 1999, **1**, 319–323.